#669

Earth Sc

NIMBUS 7

ERB ENHANCED RESOLUTION WFOV DATA TAPE

78-098A-07P

ESRB-00023

Table of Contents

1. Introduction

2. Errata/Change Log

3. LINKS TO RELEVANT INFORMATION IN THE ONLINE NSSDC INFORMATION SYSTEM

4. Catalog Materials

    a. Associated Documents

    b. Core Catalog Materials

---

1. INTRODUCTION:

The documentation for this data set was originally on paper, kept in NSSDC's Data Set Catalogs (DSCs). The paper documentation in the Data Set Catalogs have been made into digital images, and then collected into a single PDF file for each Data Set Catalog. The inventory information in these DSCs is current as of July 1, 2004. This inventory information is now no longer maintained in the DSCs, but is now managed in the inventory part of the NSSDC information system. The information existing in the DSCs is now not needed for locating the data files, but we did not remove that inventory information.

The offline tape datasets have now been migrated from the original magnetic tape to Archival Information Packages (AIP's).

A prior restoration may have been done on data sets, if a requestor of this data set has questions; they should send an inquiry to the request office to see if additional information exists.

2. ERRATA/CHANGE LOG:

NOTE: Changes are made in a text box, and will show up that way when displayed on screen with a PDF reader.

When printing, special settings may be required to make the text box appear on the printed output.

Version	Date	Person	Page	Description of Change
01				
02				

3 LINKS TO RELEVANT INFORMATION IN THE ONLINE NSSDC INFORMATION SYSTEM:

http://nssdc.gsfc.nasa.gov/nmc/

[NOTE: This link will take you to the main page of the NSSDC Master Catalog. There you will be able to perform searches to find additional information]

4. CATALOG MATERIALS:

a. Associated Documents To find associated documents you will need to know the document ID number and then click here. http://nssdcftp.gsfc.nasa.gov/miscellaneous/documents/

b. Core Catalog Materials

REQ. AGENT	RAND NO.	ACQ. AGENT
DHG		CYN

NIMBUS 7

ERB ENHANCED RESOLUTION WFOV DATA TAPE

78-098A-07P ESRB-00023

This data set catalog consists of 1 magnetic tape. The tape is 1600 BPI, 9-track, multifiled and created on an IBM 360 computer. The first file is an EBCDIC header file, followed by 12 monthly data files and 46 8-day data files. The D and C number and the time span are as follows:

D#	C#	FILES	TIME SPAN
D-78801	C-26821	59	07/01/83 - 07/02/84

B R I E F D E S C R I P T I O N
8+30d Avg WFOV Albedo,Olr+Net Rad
78-098A-07P

The Nimbus-7 Earth Radiation Budget (ERB) WFOV 8-day and Monthly7 dataset consists of enhanced resolution of earth radiation budget data. The data set was generated from the Solar Earth Flux Data Tape (SEFDT, NSSDC ID 78-098A-07B) It contains 8-day and monthly averaged albedos, outgoing longwave radiation (OLR) and net radiation that are retrieved from the wide-field-of-view (WFOV) shortwave radiometric measurements using a deconvolution algorithm. The parameters are described by truncated spherical harmonic expansions, taking into account the large amount of oversampling (a measurement every 4 s) along the orbital track. In comparison to the WFOV parameters on the ERB MATRIX tapes (NSSDC ID 78-098A-07C), the resultant deconvolved maps more correctly show the position and amplitude details of the tropical/mid-latitude albedos and OLR. Even though the quality of the data is superior, buget limits prevented the Nimbus Project from producing more than one year (July 1983 - June 1984) of them.

M A T E R I A L S F O R D I S T R I B U T I O N
78-098A-07P
8+30d Avg WFOV Albedo,Olr+Net Rad

Hucek, R., H. L. Kyle, and P. Ardanuy, "Nimbus-7 ERB Enhanced Resolution WFOV Data Tape User's Guide and Tape Specifications Document", DRAFT, September 1988 (B41887-000A).

A C K N O W L E D G E M E N T S

When using the data in any reports, publications, or presentations, please acknowledge the National Space Science Data Center and the following individuals or groups:

78-098A-07P
Dr. H. L. Kyle, Nasa/Gsfc, Dr. Herbert Jacobowitz, Noaa/Nesdis, And Members Of The Erb Nimbus Experiment And Information Processing Teams

78-084-07P
B41887

Preliminary Draft

NIMBUS-7 ERB ENHANCED RESOLUTION WFOV DATA TAPE USER'S GUIDE AND TAPE SPECIFICATIONS DOCUMENT

Richard Hucek

H. Lee Kyle

Philip Ardanuy

Space Data and Computing Division
Information and Analysis Facility
NASA/Goddard Space Flight Center
Greenbelt, MD 20771

September 1988

N8-028A-07P
B41887-00

NIMBUS-7 ERB ENHANCED RESOLUTION WFOV DATA TAPE USER'S GUIDE AND TAPE SPECIFICATIONS DOCUMENT

Richard Hucek
Research and Data Systems
10300 Greenbelt Road
Lanham, MD 20706

H. Lee Kyle
Space Data and Computing Division
Information and Analysis Facility
NASA/Goddard Space Flight Center
Greenbelt, MD 20771

Philip Ardanuy
Research and Data Systems
10300 Greenbelt Road
Lanham, MD 20706

September 1988

TABLE OF CONTENTS

Section		Page
I.	TECHNICAL BACKGROUND	1
	1. Introduction	1
	2. Model of a WFOV Shortwave Measurement	2
	2.1 In Terms of Instantaneous TOA Flux	2
	2.2 In Terms of Mean-Daily Albedo	2
	3. Method of Solution	5
	3.1 Expansion in Spherical Harmonic Functions	5
	3.2 Constraint Equations	5
	3.3 Weighted Least Squares Solution	6
	3.3.1 The Constraint Equation Weights	6
	3.3.2 The Measurement Equation Weights	9
	4. Representative Deconvolution Results	10
	5. Time Series Analysis	10
	6. Conclusions	14
II.	DATA SOURCES	14
III.	TAPE CHARACTERISTICS	17
	1. Tape Summary Description	17
	2. Header File	17
	3. The Data Files	18
	4. The Spherical Harmonic Coefficients	20
	5. WFOV Archived Albedo Estimate	21
REFERENCES		22

I. TECHNICAL BACKGROUND

1. INTRODUCTION

Satellite-borne wide-field-of-view (WFOV) radiometers view the entire visible Earth disk from their orbiting platforms in space. This is a desireable feature of an Earth radiation budget (ERB) instrument since the radiometer, with its horizon-to-horizon view, samples all upwelling radiances arriving at its location in space. In the case of radiometers having a flat-plate cosine angular response function, the measurement values provide a direct estimate of instantaneous outgoing flux. By application of space- and time-averaging methods, these measurements yield global estimates of emerging flux at satellite altitude. These we interpret as the radiative output of their source, the Earth.

In addition to their fundamental interpretation as instantaneous outgoing fluxes at satellite altitude, WFOV observations can be modeled by a two-dimensional integral across the radiometer FOV. Inversion of the integral equation leads to parameter field estimates at the top of the atmosphere (TOA). Smith and Green (1981) have shown how a set of WFOV measurement equations can be inverted by deconvolution to yield the TOA distribution of longwave radiation. There is, however, a fundamental limit to the spatial resolution achievable through deconvolution. By means of simulation studies, Hucek et al. (1987) and Ardanuy et al. (1987) have investigated the effect on resolution of spatial aliasing of temporal variability at the TOA during the course of a complete WFOV sampling cycle. For the Nimbus-7 satellite they have found that deconvolution leads to a spatial resolution corresponding to a spherical cap of about a 7° radius at the TOA. This is not as good as that obtainable by means of narrow-field-of-view (NFOV) radiometers which infer TOA fluxes from angular reflectance models and/or multiple radiance observations of the same region. Nevertheless, scanning NFOV radiometers have failed in the past on account of mechanical difficulties. The more reliable WFOV sensors then provide the only means for deriving long-term records of regional, TOA ERB parameters. A case in point is that of the ERB instrument package carried aboard Nimbus-7. After 18 months of operation, the NFOV scanning motor drive suddenly failed in June of 1980. During the succeeding years, only the WFOV radiometers have viewed such climatologically important episodes as the El Chichón eruption in April of 1982 and the El Niño/Southern Oscillation (ENSO) event of 1982-1983. To study climate changes related to these events, in-situ observations (i.e., at the TOA) of radiant exitances are most useful. This provides the major impetus for the deconvolution of Nimbus-7 WFOV observations.

In the following we present a WFOV deconvolution strategy which is equally applicable to both longwave and shortwave radiometer measurements. The two problems differ, however, in several important aspects. Among these are: (1) that the desired TOA flux field varies within three orders of magnitude for shortwave radiation, whereas for longwave radiation it varies within one; (2) for the shortwave problem there is an Earth terminator present beyond which no solar illumina-

tion falls and associated parameter fields (viz. albedo) are undefined; and (3) strong diurnal and anisotropic reflection, in the case of shortwave radiation, preclude an assumption of isotropy in describing the hemispherical distribution of outgoing radiances. For longwave radiation, on the other hand, nearly isotropic emission from the TOA has been observed from satellite observations (Taylor and Stowe, 1984, 1986). If this assumption is carried through to the deconvolution method, then the longwave problem can also be solved by the method of Smith and Green (1981). Here we shall concentrate on illustrating a deconvolution method for the more general shortwave problem. Procedures for treating the characteristics of the reflected shortwave flux field are introduced together with a representative set of resultant TOA deconvolved fields. Finally, the utility of the deconvolved fields is tested by considering the detection of the 30- to 60-day mode oscillations in the tropics.

2. MODEL OF A WFOV SHORTWAVE MEASUREMENT

2.1 IN TERMS OF INSTANTANEOUS TOA FLUX

A WFOV satellite observation is modeled as the convolution over the radiometer field of view (FOV) of the product of the incoming radiance with the instrument angular response function. This is expressed as

$$F_{sat} = \int_{FOV} R_{TOA} \cos(\eta)\, d\Omega \tag{1}$$

where F_{sat} is the measured flux at satellite altitude, R_{TOA} is the outgoing radiance field at the TOA, η is the incoming nadir angle at the satellite, and $\cos(\eta)$ is the flat plate cosine response characteristic of the Nimbus-7 WFOV radiometers. Since we desire the TOA distribution of reflected flux, the radiance from any scene is expressed as

$$R_{TOA} = \rho\, F_{TOA} \tag{2}$$

where F_{TOA} is reflected flux and ρ is a scene-dependent anisotropic reflectance model. It accounts for the nonuniform angular distribution of reflected flux over the outgoing hemisphere. Using Eq. (2) in Eq. (1), the instantaneous flux at satellite altitude is related to the instantaneous flux at the TOA by

$$F_{sat} = \int_{FOV} \rho\, F_{TOA} \cos(\eta)\, d\Omega \tag{3}$$

2.2 IN TERMS OF MEAN-DAILY ALBEDO

The measurement model of Eq. (3) is not the most convenient for deconvolution since the unknown, F_{TOA}, varies broadly in phase and amplitude with the large pole-to-pole gradient in solar insolation, I. Since the solar insolation is known from geometric considerations, it may be introduced into Eq. (3) by expressing F_{TOA} as

$$F_{TOA} = a\, I, \tag{4}$$

where a, the instantaneous albedo, becomes the unknown parameter field. However, the albedo field common to all measurements is not a, but rather $\bar{a}$, the diurnally averaged or mean daily albedo. These are related by

$$a = m\, \bar{a}, \tag{5}$$

where m is a field of diurnal models which depend both on the instantaneous scene type and its variation with time. Since scene type was not known continuously throughout the sampling period, the instantaneous m of Eq. (5) is expressed as the sum of a mean model, $\bar{m}$, and a deviation, ϵ. This we write as

$$m = \bar{m} + \epsilon \tag{6}$$

where the mean model is based upon a composite of five primary scene types (viz. ocean, land, desert, cloud, and snow/ice) as defined by Taylor and Stowe (1984, 1986); these are combined in proportion to their frequency of occurrence to form an average scene type at each field point. When the average scene is assumed to apply at each observation, random errors with a nonzero mean will result. The biases are due primarily to inadequacies of the 5-scene composite models to describe all existing scene types and to correlations of scene type with time of day such as the emergence of tropical cloud fields during the early afternoon. In the latter instance, a series of daily observations collected at the same local time for the same subsatellite position will not view the variety of scene types that occur throughout the diurnal interval and lead to an unbiased model. Rather, that scene which is present at the local time of observation is preferentially viewed. For the Sun-synchronous orbit of Nimbus-7, most of the Earth is viewed within one hour of local noon or midnight. This is shown in Figure 1, where the local time of satellite overpass is given as a function of latitude. We note that observations are taken within one hour of local noon as the satellite moves from 60°S to 50°N latitude on its ascending node and within one hour of local midnight in moving from 60°N to 50°S latitude on descending node. Toward the poles the satellite is seen to make a rapid transition in local hour angle even though its latitudinal position is scarcely changing. In this region the suborbital track has reached its meridional extreme so that the satellite velocity vector is directed along a latitude circle. As a consequence, its longitude and local hour angle are changing rapidly especially with the convergence of meridians toward the poles. This region of strongly varying local hour angle, however, is restricted to about 30° of the poles. The remainder of the Earth is viewed near local noon and midnight. A systematic scene misidentification, with respect to a daily mean scene, is likely to occur for a Sun-synchronous orbiter such as Nimbus-7 and a nonzero bias error may result.

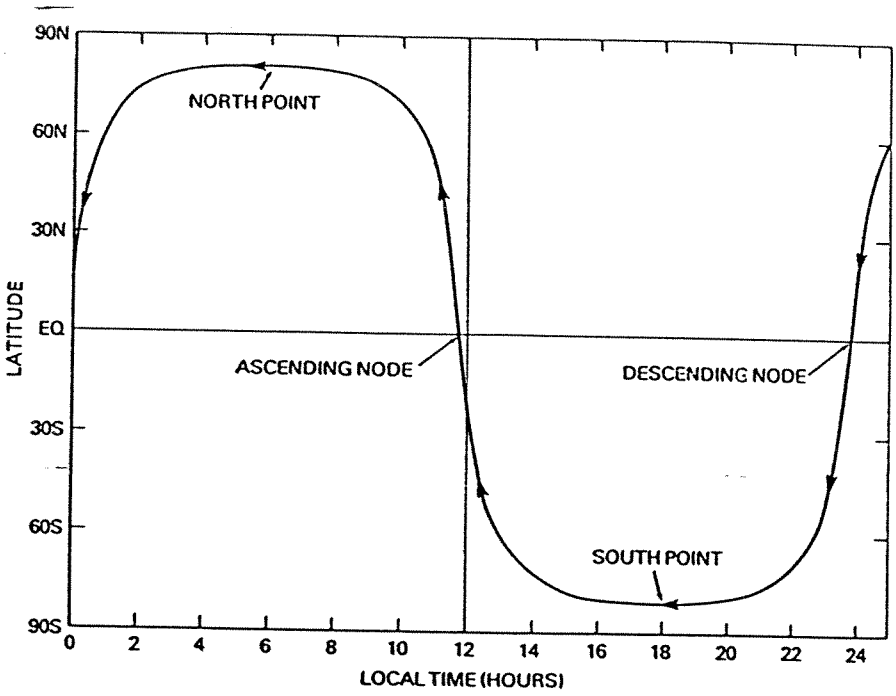

FIGURE 1. The orbit of the Nimbus-7 satellite in latitude/local time space. By design, the ascending node is near local noon; most daytime observations (between 50°N and 60°S) are taken within an hour of local noon.

Combining Eqs. (3), (4), (5), and (6) and using a mean model for ρ as well as m, we obtain

$$F_{sat} = \int_{FOV} \bar{\rho}\ \bar{m}\ \bar{a}\ I \cos(\eta)\ d\Omega + \Delta\epsilon. \qquad (7)$$

In Eq. (7) the model of a shortwave measurement has been transformed to a representation in terms of $\bar{a}$. An advantage over a representation in terms of $\bar{F}_{TOA}$ is presumed since the inversion will now recover only information not already known by other means. The random scene-related errors, $\Delta\epsilon$, that occur in the measurement model incorporate the combined errors in $\bar{\rho}$ and $\bar{m}$ and are not further analyzed in our formalism; they appear only as noise with a possible nonzero mean.

3. METHOD OF SOLUTION

3.1 EXPANSION IN SPHERICAL HARMONIC FUNCTIONS

The unknown albedo $\bar{a}$ of Eq. (7) is expressed as a truncated spherical harmonic series over the illuminated portion of the Earth. We write

$$\bar{a} = \sum_{k=1}^{N} A_k Y_k \tag{8}$$

where the A_k are unknown expansion amplitudes and the Y_k are spherical harmonic functions. In the region of total darkness near the winter pole, the albedo is undefined and the expansion of Eq. (8) does not apply. As a result, the spherical harmonic functions, while forming a complete set for any region of the globe, are a nonorthogonal basis set when applied to only a portion of the Earth as in this study. A consequence of this is that the expansion coefficients will depend on the length, N, of the summation. Nevertheless, the series representation for $\bar{a}$ leads to a reproducible field for any choice of N. In this paper, N includes all spherical harmonic terms in a rhomboidal expansion of 15 meridional nodes for each of 8 zonal waves and the mean.

When Eq. (8) is substituted for $\bar{a}$ in Eq. (7), a linear equation in the unknown expansion amplitudes results. We have

$$F_{sat,i} = \sum_{k=1}^{N} M_{ik} A_k \tag{9}$$

where M_{ik} is a matrix element for the i^{th} equation and k^{th} unknown amplitude given by

$$M_{ik} = \int_{FOV_i} \bar{\rho}\, \bar{m}\, Y_k\, I \cos(\eta)\, d\Omega. \tag{10}$$

3.2 CONSTRAINT EQUATIONS

Due to the 6-day repeat cycle of the Nimbus-7 sampling pattern, a time-averaging error is committed by assuming that the average of the observed satellite fluxes is equal to the actual period mean flux as represented by the integral of Eq. (7). At low spectral resolution, the inversion of this noise is automatically suppressed and does not affect the solution. At high resolution, an auxillary method of noise suppression is required. This we accomplish by introducing constraints in the form of other linear equations in the unknown expansion amplitudes. The constraints represent known properties of the solution and are included, along with the measurement equations, as part of the system description.

There are two objectives in the use of constraints in this problem. One is to control the inflation and instability of the solution vector **A** caused by the inversion of sampling noise. In this

case we look for a solution vector with components of relatively small magnitude. This condition can be approached through ridge regression in which we demand for each unknown amplitude

$$A_k = 0 \qquad k = 1, N. \tag{11}$$

A second objective of the constraints is to ensure the proper meridional boundary behavior of the solution at the north and south extremes of the Nimbus-7 sampling pattern. Here we require that the meridional curvature of the zonal mean be reasonably small for the illuminated portion of the Earth. This characteristic is approached through the condition

$$d^2\bar{a}/d\theta^2 \,|_{\theta=\theta_i} = 0 \tag{12}$$

where θ is latitude and i represents one of 40 possible zonal bands. The zeros of the constraint equations are not meant to represent plausible values for these conditions, but only to provide a convergence limit in the direction of which a reasonable solution must lie.

3.3 WEIGHTED LEAST SQUARES SOLUTION

3.3.1 The Constraint Equation Weights

The measurement and constraint equations are solved simultaneously for the A_k by minimizing the weighted least-squares error given by

$$E^2 = \sum_{i=1}^{M} w_i^2 \left(F_i - \sum_{k=1}^{N} M_{ik} A_k\right)^2 \tag{13}$$

In Eq. (13) the constraint equations, assumed to be written in the matrix form of Eq. (9), are included in the outer summation along with the measurement equations for a total of M equations, and the F_i are generalized measurement values including both the satellite and constraint values. Realistic solutions are chosen from a sequence of results obtained by varying the weighting factors, w_i, of the constraint equations between zero (unconstrained) and infinity (the null solution). Suitable values for these weights are determined by comparing features of the retrieved solutions to a priori known characteristics of the Earth albedo and to lower-resolution results obtained by other methods (Jacobowitz et al., 1984). Figures 2, 3, and 4 illustrate the empirical procedure that we have used to derive the monthly mean albedo for December 1983 for the case of the ridge constraints. Figure 2 shows the result of a lower-resolution solution termed the WFOV archived albedo. It depicts patterns of high and low albedo that appear within the tropics and mid-latitudes and that must also exist in the deconvolved result. Figure 3 is a deconvolved solution but without the application of ridge constraints. It brings out the large-scale patterns of albedo ridges and troughs as were seen in the archived albedo and, in addition, reveals several high resolution features not previously discernible. The emergence of an albedo ridge across the equatorial Pacific, for example, is noted in the deconvolved result. This new detail is acceptable as a valid feature

of the Earth albedo since it corresponds to the known cloud fields along the Intertropical Convergence Zone (ITCZ). The unconstrained result, however, exhibits instability near the terminator, as seen by the large amplitude waves at 65°N. These have been subdued in Figure 4 with the application of the ridge constraints. This solution preserves all the features of the previous unconstrained result within the tropics and mid-latitudes, with the addition that it has a plausible behavior near the terminator where incident insolation drops to the level of noise.

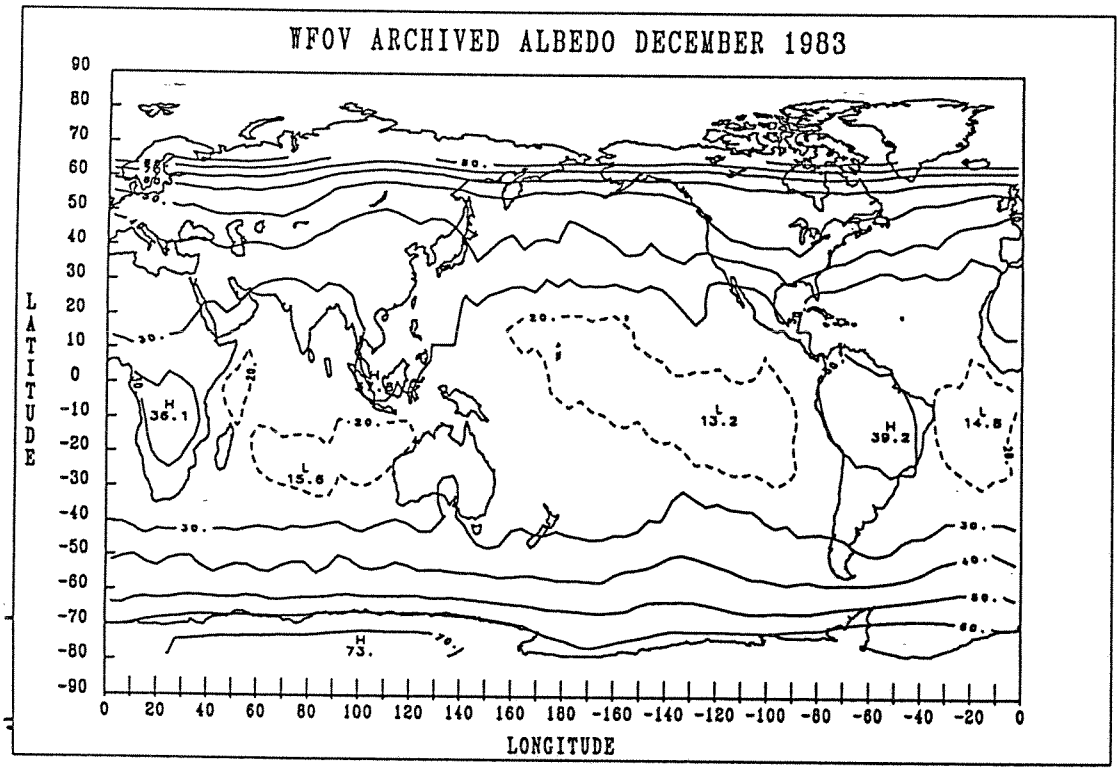

FIGURE 2. WFOV archived, mean-daily albedo (%) for the month of December 1983.

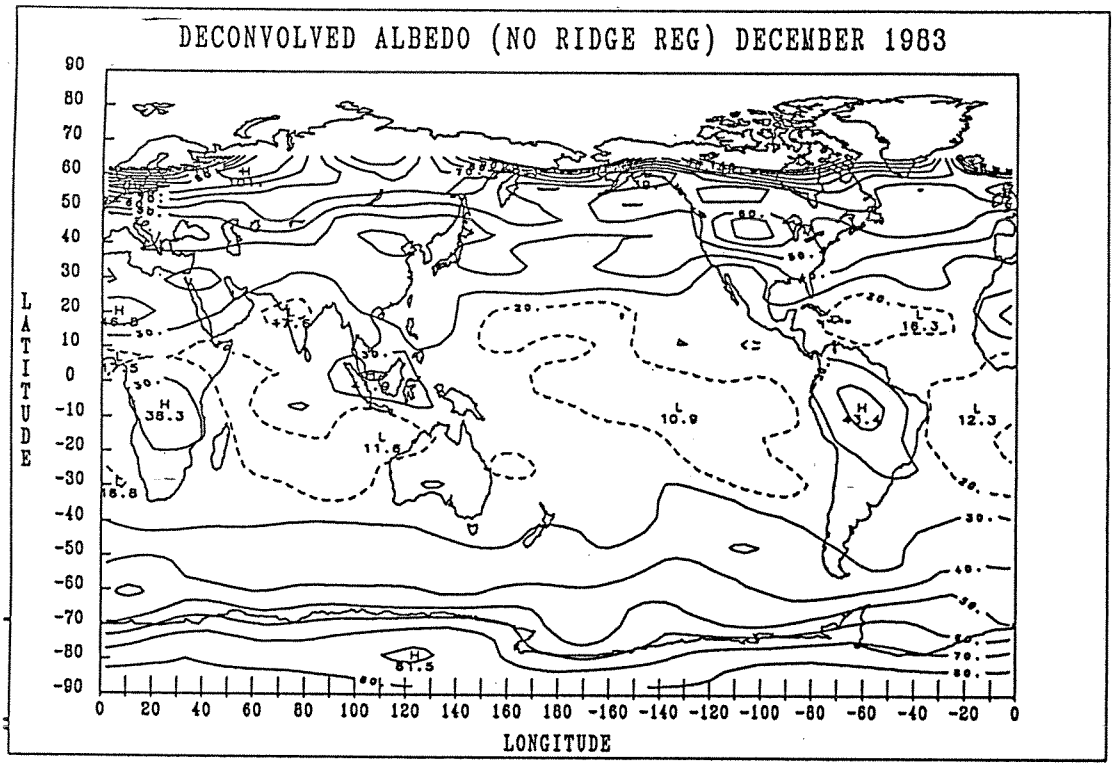

FIGURE 3. Deconvolved, mean-daily albedo (%) without ridge regression constraints for the month of December 1983.

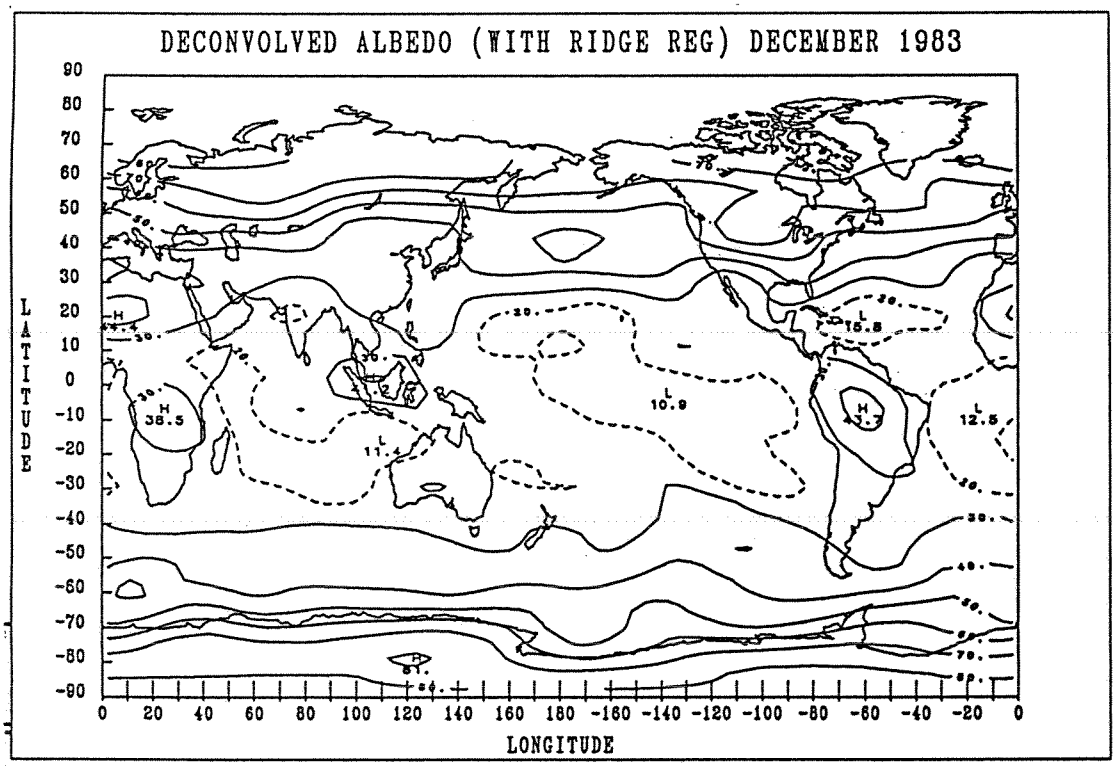

FIGURE 4. Deconvolved, mean-daily albedo (%) with ridge regression constraints for the month of December 1983.

Table 1 contains a summary of the meridional and ridge equation weight factors that we have used in obtaining 8-day mean fields of albedo. They are given in the form

$$w_i = \lambda \, v_i \tag{14}$$

where λ is a common magnification factor and v_i is a relative factor for the weights of a given constraint type. The variables m and n that appear in the table are, respectively, the number of zonal waves and meridional nodes represented by a given term of a spherical harmonic series and which are also used to obtain the relative weight factor, v_i. θ is latitude.

TABLE 1. INVERSION WEIGHTS FOR THE CONSTRAINT EQUATIONS

Constraint Type	λ	v_i	w_i
Ridge	100	$m_i + n_i$	$100 \cdot (m_i + n_i)$
Meridional Smoothing	8	$\sin^2(\theta_i)$	$8 \cdot \sin^2(\theta_i)$

3.3.2 The Measurement Equation Weights

For the satellite measurement equations, weight factors are derived by noting that the mean-reflected flux is related to the mean albedo and insolation, $\overline{I}$, by

$$\overline{F}_{TOA} = \overline{a} \, \overline{I}. \tag{15}$$

When Eq. (15) is used in Eq. (7), the satellite measurements may be expressed in terms of $\overline{F}_{TOA}$. Furthermore, according to the mean value theorem for integrals, a solution for $\overline{F}_{TOA}$ at an undetermined point, x, within the FOV may be extracted from the integral and is given by

$$\overline{F}_{TOA}(\mathbf{x}) = F_{sat} \left\{ \int_{FOV} \overline{\rho} \, \overline{m} \, (I/\overline{I}) \cos(\eta) \, d\Omega \right\}^{-1} \tag{16}$$

Equation (15) shows that a satellite measurement value may be converted to an equivalent mean flux measurement value at the TOA by scaling with the term in brackets. This is important because the factor $(\overline{I}/I)$ scales an observation in proportion to its mean-daily solar insolation. This allows the least-squares procedure to minimize the errors in the albedo solution as weighted by the mean-daily illumination rather than the instantaneous insolation at the time of the observations (which is satellite-dependent). Similarly, the model of a satellite measurement may be converted to the model of a TOA measurement by the same scaling factor. The TOA equivalent measurements and models are not useful individually since the point x remains

unknown. However, the scaling factors can be applied to the measurements equations as least-squares weights. They transform the inversion problem from a minimization of flux error at satellite altitude to a minimization at the TOA.

4. REPRESENTATIVE DECONVOLUTION RESULTS

In Figures 5 and 6 we compare global TOA maps of the WFOV archived and deconvolved albedos, respectively, for the 8-day period from August 10, 1983 through August 17, 1983. The archived result exhibits the general pattern of peaks and valleys that can be discerned by the WFOV radiometers and which must appear in the deconvolved result. It, however, is plagued by an extremely tight gradient in albedo as we approach the region of total darkness in the southern hemisphere. There the albedo is seen to rise above the physically acceptable limit of 100 percent. Elsewhere the archived result appears noisy, especially in the southern hemisphere mid-latitudes between 30° and 60° south latitude.

The deconvolved albedo, on the other hand, has suppressed the noise apparent in archived solution and yields a physically admissible albedo even to the terminator boundary. This is, in part, due to the inclusion of anisotropic reflection in the measurement model which can account for relatively large WFOV measurements through the preferential forward scattering of radiation toward the satellite. This is particularly true when the satellite is near the terminator and able to view the large forward beam that occurs for reflection at high local-solar zenith angles of incidence. Throughout the tropics and mid-latitudes we notice the enhanced resolution of the deconvolved field by the magnification of the ridge-to-trough amplitudes that occur. Also evident is the clarification of finer structure such as the cut-off high over Greenland, the track of the ITCZ across the equatorial Pacific, and the shape of the South Pacific Convergence Zone from southeast Asia through Borneo and the New Guinea and east of Australia.

5. TIME SERIES ANALYSIS

A time-longitude section along the equator of a one-year sequence of 8-day deconvolved albedo fields is shown in Figure 7 for the period July 1983 through June 1984. The time series consists of 46 8-day mean fields for a latitude band of 9° centered about the Equator. It represents a raw data field which, when time-filtered, will be analyzed for eastward propagating wave modes. From the figure we immediately recognize three zones of relatively high albedos extending from 10° to 30° east, 60° to 150° east, and 60° to 90° west longitude. These regions are characterized by deep convective activity and correspond, respectively, to the Congo River basin of Africa, the Indian Ocean south of India eastward through Indonesia (Asian monsoon), and the Amazon River basin of South America. The large albedos in these cases arise from the copious high cloud amounts produced by convection. Especially notable are the periodic impulses of high albedo over the Amazon which may be linked to convective outbreaks occurring elsewhere (Lau and Chan, 1985). Between these areas are the

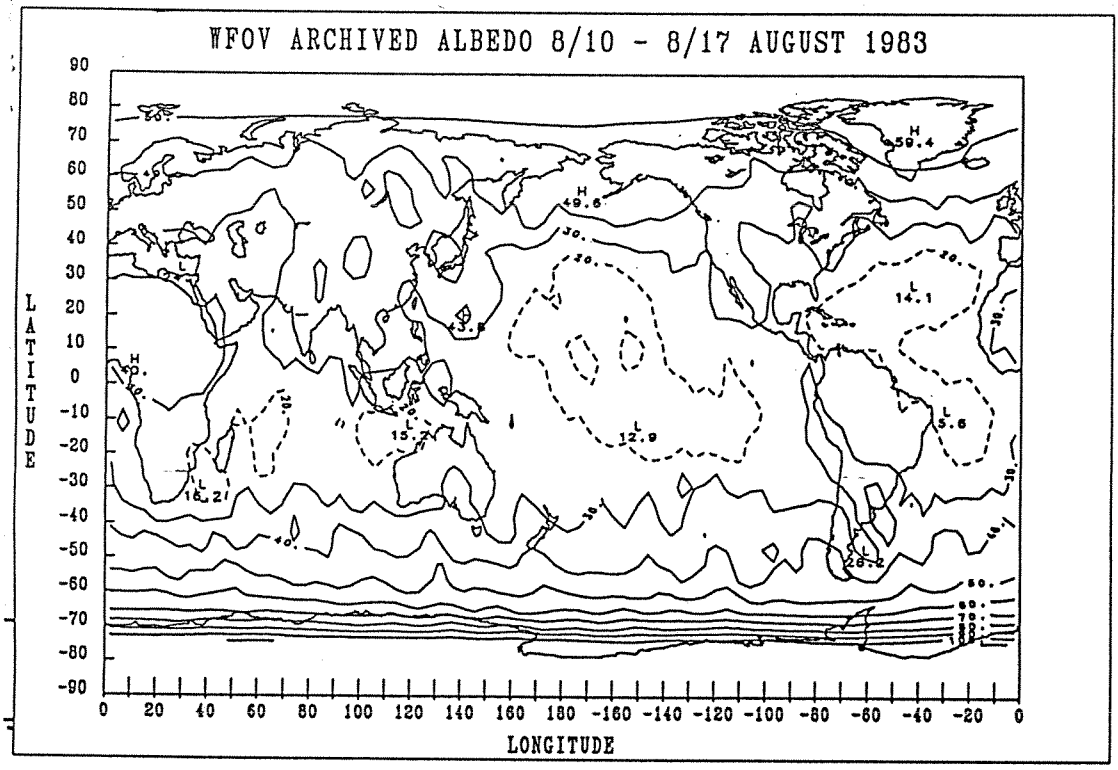

FIGURE 5. WFOV archived, mean-daily albedo (%) for the 8-day period August 10, 1983 through August 17, 1983.

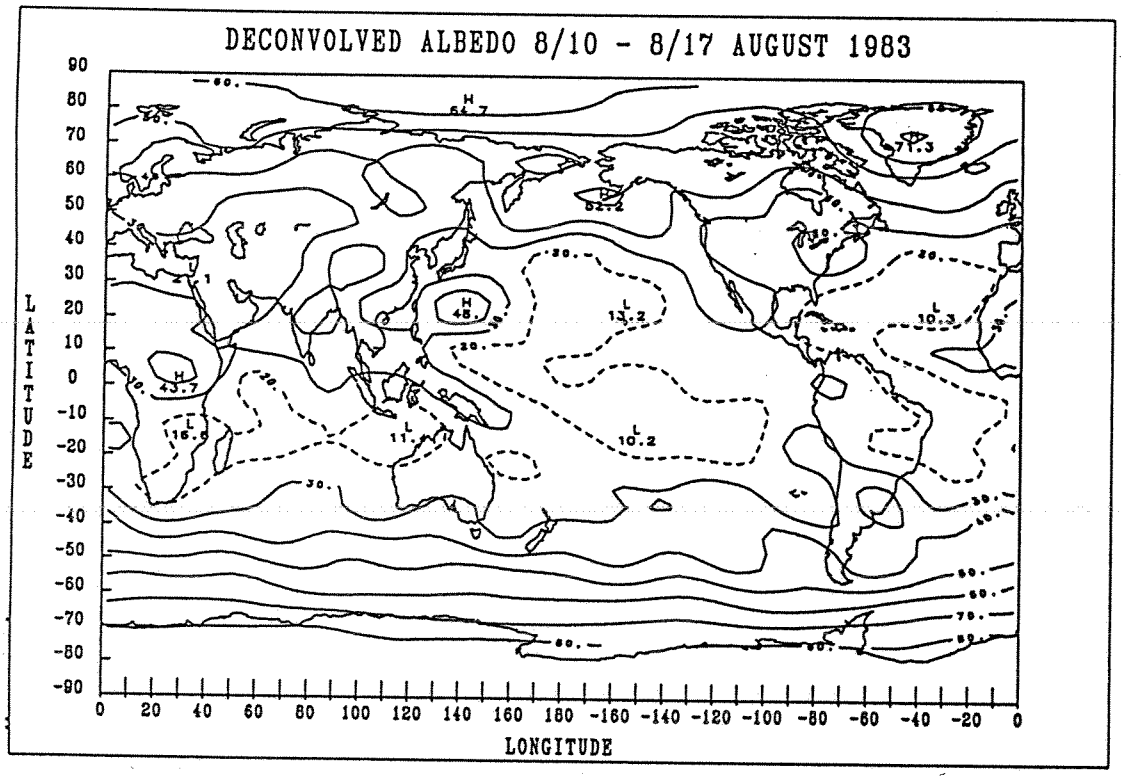

FIGURE 6. Constrained, deconvolved, mean-daily albedo (%) for the 8-day period August 10, 1983 through August 17, 1983.

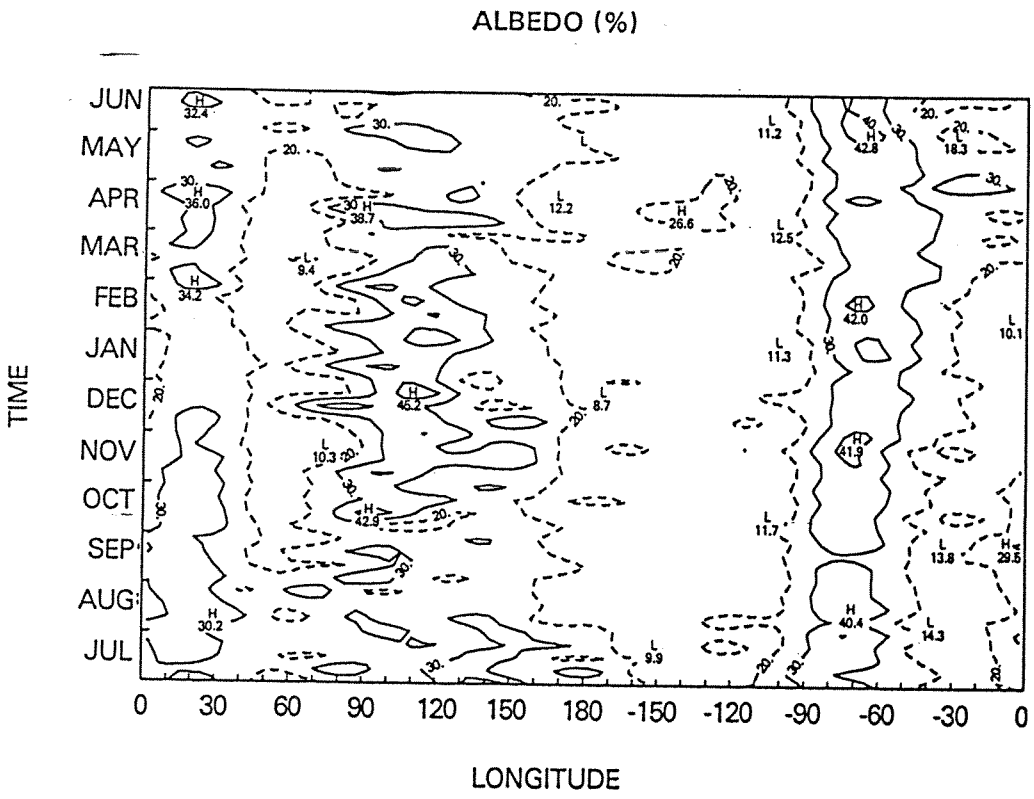

FIGURE 7. Time-longitude section of 8-day mean fields of deconvolved albedo (%). The time series extends from July 1983 through June 1984 and represents the average albedo within a 9-degree latitude band centered about the Equator.

relative quiescent regions of lower albedo corresponding to the south Arabian Sea, Pacific Ocean, and Atlantic Ocean.

In Figure 8 are shown the results of applying a band pass filter to the data of Figure 7. The time series at each of 80 equally spaced longitudinal positions has been filtered to pass mainly 40- to 60-day modes of oscillation while other frequencies are suppressed. The precise frequency response of the first-order Butterworth filter is included in Table 2. After filtering, the resultant time series are reconstructed on a Hovmöller chart to consider the detection of eastward propagating waves in the tropics. These correspond to contours whose orientation lies in the direction from lower left to upper right. In the convective regions of the Asian monsoon and Amazon River basin, the contour patterns suggest a tendency toward eastward motion over a limited longitudinal length. Especially near the Amazon River the broken patterns display the presence of eastward-moving orientations. We find that the filtered time series, which retains power only in the 40- to 60-day range of periodicities, explains almost 50% of the variance of the total signal near certain longitudes. In particular, near the Congo and Amazon River valleys, and over regions of the Pacific and Indian Oceans. The limited spatial extent of the contours shown may be due to the movement of such waves in the meridional direction out of the 9° equatorial band that we have analyzed.

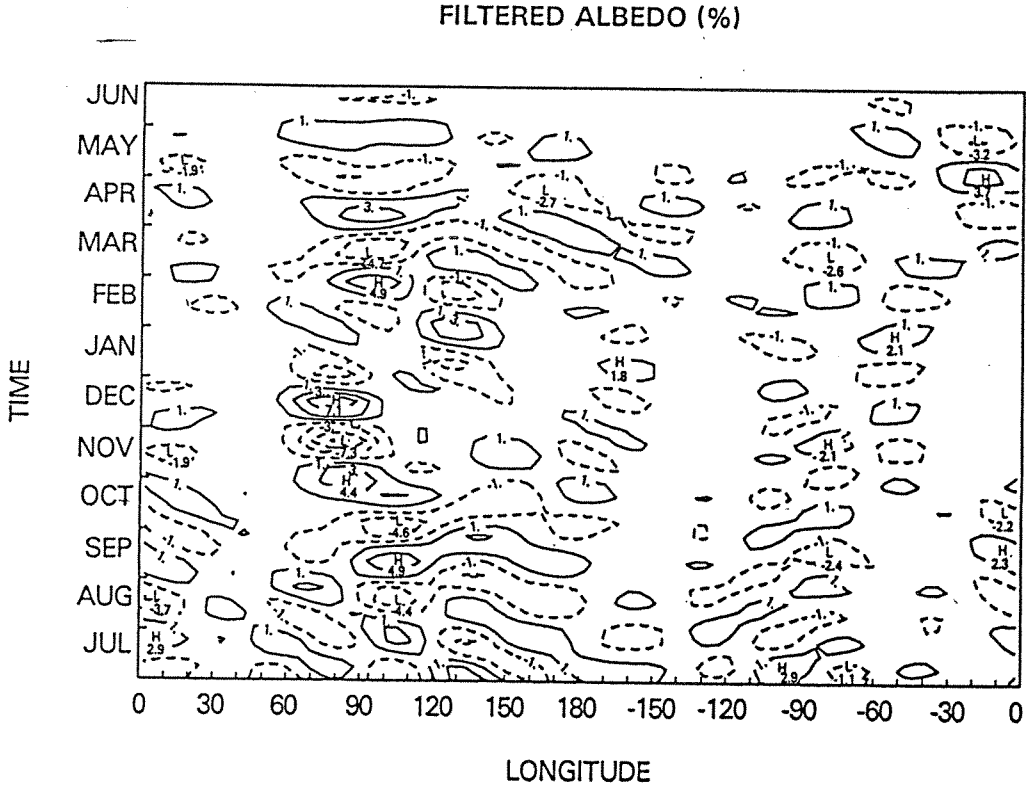

FIGURE 8. Filtered time-longitude section of 8-day mean fields of deconvolved albedo (%). The one-year time series at each of 80 longitudinal positions has been filtered to pass mainly 40- to 60-day frequency modes. The residual signals are shown from July 1983 through June 1984 along a 9-degree latitude band centered about the Equator.

TABLE 2. BAND PASS FILTER RESPONSE

Period (days)	Response (% Amplitude Retained)
16	0
30	24
35	50
45	100
60	50
75	24
90	14
105	9
120	7

6. CONCLUSIONS

The deconvolution of WFOV shortwave radiometer measurements has been demonstrated by using the ERB observation data set collected on board the Nimbus-7 satellite. Three major aspects of the shortwave problem were treated which have no analogous significance for the more tractable longwave inversion. First, the large-scale variations in magnitude of the unknown TOA-reflected shortwave field are strongly influenced by the known distribution of incident insolation. This signal is removed from the reflected shortwave radiation by expressing the latter as the product of albedo and insolation. The albedo becomes the unknown parameter field. Second, the Earth's terminator is handled by the use of constraint equations which guide the solution to a physically reasonable result even though the signal-to-noise ratio approaches zero. Finally, the strong directional and bidirectional reflectance properties of shortwave radiation are accounted for by means of scene identification and the application of corresponding angular dependence models. When the solution fields obtained by the deconvolution method are compared to lower-resolution results, we immediately notice the suppression of noise, a realistic boundary behavior at the terminator, magnification of ridge-to-trough amplitudes, and the modification of large-scale albedo patterns.

The deconvolution algorithm has been used to create a one-year sequence of 8-day mean albedos for the period from July 1983 through June 1984. The evolving fields which emerge were analyzed for the detection of 40- to 60-day eastward-propagating modes in the tropics. It appears that these waves are discernible in the deconvolved data set in the regions of the Asian monsoon and the Amazon rain forest. They may also move meridionally north and south so that they appear within the 9° latitudinal zone that we have analyzed for only a limited time. Similar analyses of adjacent latitudinal bands is required to demonstrate this supposition.

II. DATA SOURCES

The model of a WFOV shortwave observation given in Eq. (7) is fully deterministic, apart from the unknown albedo, provided the measurement value, radiometer FOV, and the distributions of incident insolation and scene-dependent angular models are known across the FOV. This information was acquired primarily through the Nimbus-7 Solar Earth Flux Data Tape (SEFDT) archive product which serves as a source of calibrated WFOV measurements (global calibration) and positional information. On the SEFDT are the succession of WFOV shortwave measurement values, together with their times and subsatellite positions, corresponding to the sequence of satellite observations taken in space. The measurement value fixes the left-hand side Eq. (7), while the time and location of the satellite permit a mapping of the radiometer FOV into terrestrial coordinates. The time (year, day, and second) also fixes the subsolar position on the Earth, the intensity of solar radiation at the TOA and, along with the satellite location, the relative position between the subsolar and the subsatellite points. The only remaining unresolved quantities in Eq. (7) are

the variations of directional and bidirectional angular models within a WFOV scene.

Since the precise distribution of scene types at the TOA was not known continuously throughout a day, nor for any sampling period, it was not possible to represent exactly the diurnal model variations that occur within any single WFOV. Rather average diurnal models were used which were based upon a mean scene description. A mean scene was defined individually for each of 2070 approximately equi-area grid elements spanning the Earth's surface. This is the ERB world grid and is shown in Figure 9. The Earth is partitioned into 40 latitude zones, each 4.5° in width, and ordered from South to North Pole. The zones are further subdivided into between 3 and 80 target areas. These are numbered westward within a zone starting at Greenwich Meridian and accumulated over all zones with target area 1 bordering the South Pole and target area 2070 bordering the North Pole. Over the course of a month, surface geography was first averaged according to percent coverage of ocean, land, desert, and snow/ice. These percentages would normally be considered geographical constants except for the appearance and disappearance of snow/ice fields. These were obtained from the Air Force's three-dimensional nephanalysis (3DN) for the year April 1979 through March 1980 and were assumed to be climatologically representative of the months and years appearing in this data set. Total cloud fields were then uniformly superimposed over the surface mixture to obtain a final five-component scene description consisting of the unencumbered percentages of ocean, land, desert, snow/ice, and cloud. The total cloud fields required for this procedure were derived from the contemporary Temperature Humidity Infrared Radiometer (THIR) and Total Ozone Mapping Spectrometer (TOMS) data sets, also derived from observations collected aboard the Nimbus-7 satellite (Hwang et al., 1988).

The method of forming mean diurnal models from a composition of several scene-dependent primary models is presented in detail in Brooks et al. (1986). Here we note that two principal assumptions are used to form diurnal models from the available data sources. The first is the supposition that a directional model corresponding to a mixture of several primary scene types can be represented by a linear combination of the directional models associated with these pure scenes. The second is that the composite scene, once identified, persists throughout the day and the entire sampling period. This permits the transformation of the newly defined directional models to diurnal models. As noted in Eq. (6), these requirements cannot always be met and will, therefore, introduce a modeling error into the inversion process.

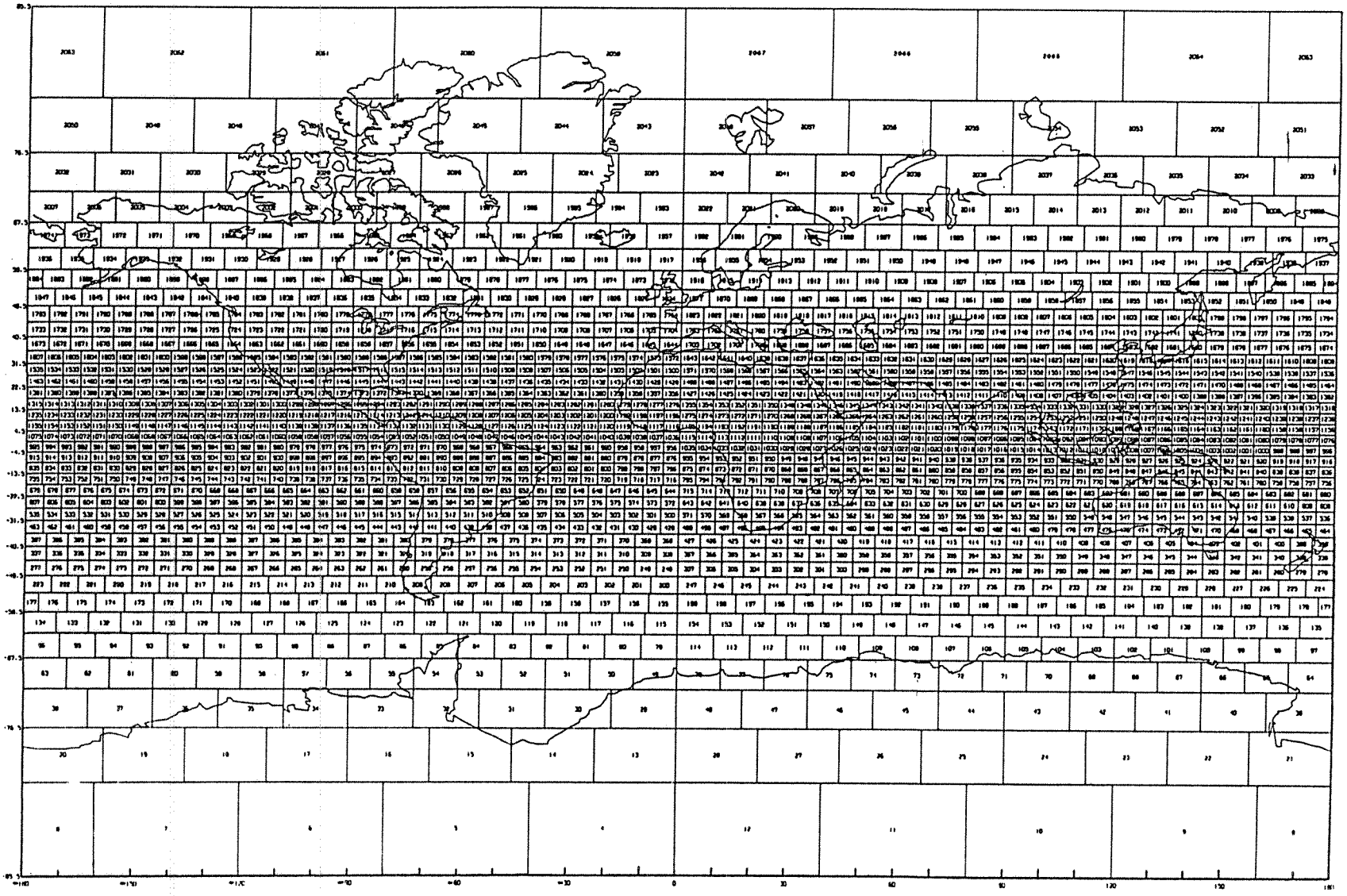

FIGURE 9. ERB world grid target areas from latitude zone 2 near the south pole to zone 39 near the north pole. Zones 1 and 40, containing the first three and last three target areas, respectively, are not shown.

III. TAPE CHARACTERISTICS

1. TAPE SUMMARY DESCRIPTION

The Nimbus-7 ERB enhanced resolution WFOV data set is stored on a single 6250-bpi no label magnetic tape. The tape contains a total of 59 files, the first of which is a standard Nimbus Observatory Processing System (NOPS) header file and the remaining 58 are data files. They consist of a progression of 12 monthly files followed by 46 8-day cyclic files covering the one-year calendar period from July 1, 1983 through July 1, 1984. The gross tape format is illustrated in Figure 10 below.

GROSS TAPE FORMAT

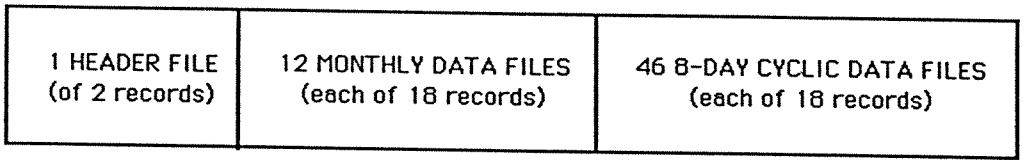

Figure 10. Gross tape format illustrating the sequence of the three file categories found on the Enhanced Resolution WFOV Data Tape. First there is a header file containing two NOPS standard header records, followed by 12 monthly data files and 46 8-day cyclic files. The data files are uniformly composed of 18 identical records.

2. THE HEADER FILE

The first file of the Enhanced Resolution WFOV Data Tape (ERWDT) is a header file containing two identical 630-byte EBCDIC character records. The 630 bytes allow complete identification of the tape in terms of its NOPS specification and sequence numbers, the data coverage interval, its generation date and time, and relevant comments describing the tape or special calibration and processing procedures used in creating it. The header file appearing on this tape is reproduced below with the subscripted '#' sign representing the blank character.

Record 1

#NIMBUS-7#NOPS#SPEC#NO#T134086#SQ#NO#AQ31821-1#ERB##SACC#TO#IPD##
START#1983#182#000000#TO#1984#183#240000#GEN#1988#215#133003#ERB#
ENHANCED#RESOLUTION#WFOV#DATA#TAPE (+ 466 BLANKS)

Record 2

#NIMBUS-7#NOPS#SPEC#NO#T134086#SQ#NO#AQ31821-1#ERB##SACC#TO#IPD##
START#1983#182#000000#TO#1984#183#240000#GEN#1988#215#133003#ERB#
ENHANCED#RESOLUTION#WFOV#DATA#TAPE (+ 466 BLANKS)

Characters 25-30 represent the 6-digit NOPS specification number while characters 38-44 define the sequence number. The data interval covered by the tape begins with the start of Julian day 182, 1983 and extends to the end of Julian day 183, 1984. This information appears in character positions 72 to 105 in the form 'YEAR#DAY#HRMNSC#TO#YEAR#DAY#HRMNSC'. The tape generation date is given by year, Julian day, hours, minutes and seconds in the form 'YEAR#DAY#HRMNSC' by characters 111-125. The remaining space within the record contains the tape title. Any additional unoccupied byte positions are filled with blanks.

3. THE DATA FILES

Each data file, whether monthly or 8-day cyclic, is composed of 18 unformatted records. These records contain the 18 parameter data fields given for each sampling period and are ordered as follows:

RECORD #	DESCRIPTION
1	spherical harmonic coefficients for the period mean albedo field (see Section 4)
2	spherical harmonic coefficients for the period mean-emitted longwave radiation field (see Section 4)
3	period mean albedo field evaluated at the 2070 ERB world grid target area centers
4	orbital (i.e., not using diurnal corrections) WFOV archived albedo estimate using the maximum reflected energy in reduction to the TOA (see Section 5)
5	deconvolved WFOV shortwave flux field evaluated at the 2070 ERB world grid target area centers
6	deconvolved WFOV longwave flux field evaluated at the 2070 ERB world grid target area centers
7	input satellite altitude WFOV shortwave measurements at 2070 world grid target areas
8	input satellite altitude WFOV longwave measurements at 2070 world grid target areas
9	reconstructed shortwave satellite measurement field using the deconvolved TOA reflected shortwave field of parameter 5
10	reconstructed longwave satellite measurement field using the deconvolved TOA emitted longwave field of record 6
11	period mean insolation field at 2070 ERB world grid target area centers

12 net radiation at 2070 ERB world grid target area centers using the deconvolved fields of records 5 and 6, and the insolation field of record 11

13 maximum possible WFOV shortwave measurement field at 2070 ERB target areas corresponding to the observed measurements of record 7. This is a computed field which is evaluated by assuming that the Earth albedo is unity (see Section 5)

14 fractional ocean coverage at 2070 target areas used to determine the mean scene composition

15 fractional land coverage at 2070 target areas used to determine the mean scene composition

16 fractional snow coverage at 2070 target areas used to determine the mean scene composition

17 fractional desert coverage at 2070 target areas used to determine the mean scene composition

18 fractional cloud coverage at 2070 target areas used to determine the mean scene composition

All 18 physical records of a data file are identical and consist of 2080 8-byte words for a total of 16640 bytes. The first 2070 words are reserved for the parameter values at the midpoints of the ERB world grid target areas. The remaining 10 words, beginning with word 2071 and continuing through word 2080, are used to supply record identification information. In the case of the first two records, however, the data values do not refer to the ERB world grid. Rather, they contain the 272 spherical harmonic expansion coefficients corresponding to the albedo and longwave fields, respectively. Of the available 2070 data words, 1798 will be unoccupied. These have been zero-filled. The record identifiers begin, as before, in word position 2071. Figure 11 illustrates a generic 2080-word physical record and its division into separate logical pieces of 2070 data words and 10 identifier words.

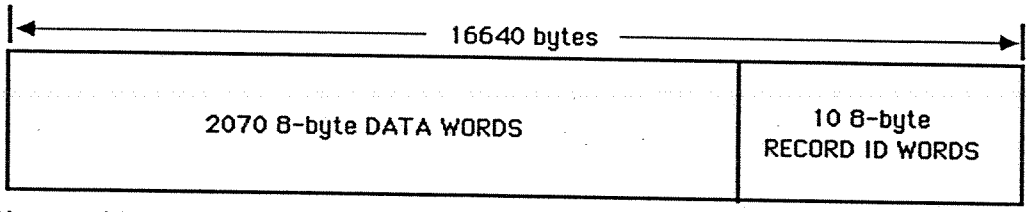

Figure 11. General physical record format of all 18 records of a ERWDT data file. There are 2070 8-byte words available for data storage and 10 8-byte words reserved for record identification information. Each record contains a total of 16640 bytes.

Of the 10 available identifiers, only the first two have been filled with useful information. The first contains the interval of the sampling period in the form: yearx10^6 + (Julian day at the start of the sampling period)x10^3 + Julian day at the end of the sampling period. For example, a sampling period extending from Julian day 335 to 365 (i.e., the month of December) of 1983 would appear as 1983335365. The second identifier contains the parameter number index, 1 through 18, as listed above.

4. THE SPHERICAL HARMONIC COEFFICIENTS

The spherical harmonic coefficients obtained by means of the deconvolution procedure pertain to a real representation of the associated albedo and longwave fields. In this instance the series solution is regenerated by combining the expansion amplitudes, C_n^m and S_n^m (also referred to as the A_k of Eq. (8)), in the form

$$f(\theta,\varphi) = \sum_{m=0}^{m} \sum_{n=m}^{m+N} C_n^m \cdot N_n^m \cdot P_n^m(\cos(\theta)) \cdot \cos(m\varphi) + \sum_{m=1}^{m} \sum_{n=m}^{m+N} S_n^m \cdot N_n^m \cdot P_n^m(\cos(\theta)) \cdot \sin(m\varphi) \qquad (17)$$

In Eq. (17), $f(\theta,\varphi)$ is an albedo or longwave field at colatitude θ and longitude φ. θ ranges in value from 0 at the North Pole to π at the South Pole while φ increases westward from 0 at Greenwich Meridian to π at the date line and decreases eastward from Greenwich Meridian to $-\pi$ at the date line. Note that this convention is opposite the traditional ordering of longitudes which increase eastward and decrease westward from Greenwich. P_n^m is an unnormalized associated Legendre polynomial of degree n and order m. For a rhomboidal truncation of M zonal waves and N meridional nodes, m will vary from 0 to M and n will vary, for each m, from m to m+N. The C_n^m are the amplitudes of spherical harmonic terms containing a cos(mφ) function. Similarly, the S_n^m are amplitudes for the terms with a sin(mφ) function. Finally, N_n^m is a normalization constant for the spherical harmonic function such that the global integral of any two spherical harmonics of indices (m,n) and (q,r) satisfy:

$$\int_{\text{sphere}} N_n^m \cdot P_n^m \cdot \cos(m\varphi) \cdot N_r^q \cdot P_r^q \cdot \cos(q\varphi) \cdot d\Omega = 4\pi \cdot \delta_n^r \cdot \delta_m^q$$

and (18)

$$\int_{\text{sphere}} N_n^m \cdot P_n^m \cdot \sin(m\varphi) \cdot N_r^q \cdot P_r^q \cdot \sin(q\varphi) \cdot d\Omega = 4\pi \cdot \delta_n^r \cdot \delta_m^q$$

The normalization constant of Eqs. (18), N_n^m, is given algebraically as:

$$N_n^m = (2n+1) \cdot (n-m)! \cdot (2-\delta_0^m)/(n+m)! \qquad (19)$$

with n being the degree of the associated Legendre polynomial, m its order, and δ_0^m the Kronecker delta function which is unity for m=0 and zero if m≠0.

Since we have used a real rhomboidal expansion of 8 zonal waves and 15 meridional nodes, there will be 9x16=144 cosine amplitudes and 8x16=128 sine amplitudes for a total of 272 coefficients. The coefficient records are structured so that first all 144 cosine amplitudes are given. These are followed by the 128 sine amplitudes. Within the cosine and sine terms the ordering is such that, for a given node, all corresponding wave terms are listed consecutively, from smallest to largest wave number. Among the nodes the ordering is again from least to greatest node number. As an example, consider the case of 8 waves and 15 nodes. The first nine coefficients correspond to node zero and wave numbers 0-8. The next set of nine coefficients (i.e., record elements 10-17) correspond to node one and again wave numbers 0-8. This pattern continues through 15 nodes with the last element of the cosine set (record element 144) corresponding to node 15 and wave 8. Beginning with element 145 the coefficients for the sine terms begin. The scheme is identical to that of the cosine coefficients, except that now there are no elements that correspond to zero wave terms (the spherical harmonic P_n^0 sin(0) is identically zero and is not included in the expansion). Hence, the next eight elements (i.e., record elements 145 through 152) correspond to node zero and waves 1-8. The sine-term coefficients continue successively through element 272 which is associated with node 15 and wave 8.

5. WFOV ARCHIVED ALBEDO ESTIMATE

The WFOV orbital albedo is obtainable from the satellite measurements by a more direct procedure than a deconvolution. In Eq. (3) we substitute (4) and write

$$F_{sat} = \int_{FOV} \rho \; a \; I \cos(\eta) \; d\Omega \tag{20}$$

where a, as before, is the instantaneous albedo field at the time of observation. When a FOV average albedo, a_{WFOV}, is extracted from the integral of Eq. (20), and the approximation is made that shortwave reflection occurs isotropically at the TOA (i.e., $\rho=1/\pi$) we may invert Eq. (20) to obtain

$$a_{WFOV} = \frac{F_{sat}}{(1/\pi) \int_{FOV} I \cos(\eta) \; d\Omega} \tag{21}$$

This is the WFOV albedo estimate. It is derived from the measurement value by dividing by the maximum possible measurement value under conditions of isotropic reflection (i.e., Eq. (20) with the albedo everywhere unity and $\rho=1/\pi$) . The latter quantity involves the integration of solar insolation field over the instantaneous FOV of the observation, a well defined geometrical problem. Eq. (21) then yields an instantaneous albedo estimate without the use of scene identification and accompanying angular dependence models. The resultant albedo field, however, is particularly likely to be

inaccurate in regions of sharp albedo change, where the FOV average is not representative of the desired albedo at the subsatellite position, and near the terminator where strong anisotropic effects undermine the assumption of isotropic reflection.

REFERENCES

Ardanuy, P. E., H. L. Kyle, R. R. Hucek, and B. S. Groveman, 1987: Nimbus 7 Earth Radiation Budget Wide Field of View Climate Data Set Improvement, 2, Deconvolution of the Earth Radiation Budget Products and Consideration of the 1982-1983 El Niño Event, J. Geophys. Res., 92, 4125-4143.

Brooks, D. R., E. F. Harrison, P. Minnis, and J. T. Suttles, 1986: Development of Algorithms for Understanding the Temporal and Spatial Variability of the Earth's Radiation Balance, Reviews of Geophysics, 24, 422-438.

Hucek, R. R., H. L. Kyle, and P. E. Ardanuy, 1987: Nimbus 7 Earth Radiation Budget Wide Field of View Climate Data Set Improvement, 1, The Earth Albedo from Deconvolution of Shortwave Measurements, J. Geophys. Res., 92, 4107-4123.

Hwang, P. H., L. L. Stowe, H. Y. M. Yeh, H. L. Kyle, and the Nimbus-7 Cloud Data Processing Team, 1988: The Nimbus-7 Global Cloud Climatology, Bull. Amer. Meteor. Soc., 69, 743-752.

Jacobowitz, J., H. V. Soule, H. L. Kyle, F. B. House, and the Nimbus 7 ERB Experiment Team, 1984: The Earth Radiation Budget Experiment: An Overview, J. Geophys. Res., 89, 5021-5038.

Lau, K. M. and P. H. Chan, 1985: Aspects of the 40-50 Day Oscillation During Northern Winter as Inferred from Outgoing Longwave Radiation, Mon. Wea. Rev., 113, 1889-1909.

Smith, G. L., and R. N. Green, 1981: Deconvolution of Wide Field-of-View Radiometer Measurements of Earth-Emitted Radiation, I, Theory, J. Atmos. Sci., 38, 461-473.

Taylor, V. R. and L. L. Stowe, 1984: Reflectance Characteristics of Uniform Earth and Cloud Surfaces Derived from Nimbus 7 ERB, J. Geophys. Res., 89, 4987-4996.

Taylor, V. R. and L. L. Stowe, 1986: Revised Reflectance and Emission Models from Nimbus-7 ERB Data, Extended Abstracts, Sixth Conference on Atmospheric Radiation, May 13-16, 1986, Williamsburg, VA (American Meteorological Society), 45 Beacon Street, Boston, MA 02108), J19-J22.

file 1 Header
file 2-13 Monthly
file 14-59 8-day
Time is at end of block

78-098A-07P

FILE 2	REC NO 1									
(0)	40572C45	CA356B0A	3F1A615C	5A1A0A1C	BF1AC356	7F70D714	3F1E34E1	C54638C3	3F37E9F8	B0864D5B
(40)	3F18FCE6	016C54E9	BF63A16F	C9B3D2FB	3F2B6601	40A771AF	3EEAF9CF	22C8C0F0	BFEA4047	EEBCC3C5
(80)	BF1B700C	153A70D8	BF1470A7	A3EC0477	3F1F440D	BF046E81	3F12D8F6	25072FD5	BF132949	3DB83825
(120)	BF6F1BCA	CA9AC6AF	5F48A018	43770231	3F592DB7	B79F4D6F	402067E1	78897863	BF21F0F9	5B42F7A2
(160)	3F167A70	1B44D149	3F407B95	CF3B2A5C	BF9B3695	7C5E2126	BE5D7A50	1C41F3F5	BE2D1EDA	5FCFCE9C
(200)	3F151082	2071DF76	3F3D090F	1720AAA3	BF842729	6FFDA4D5	BF156EEA	9AD55D54	3F25D80D	AD740C5C
(240)	BF2F7DF2	0F64CA0D	BFCA6138	C71A73EB	3E579231	4245EDB7	3E5C2C2E	E40D9D32	3E3DE2BC	29AB83D5
(280)	3F0F5128	C270B752	3F9343D8	FF0A6C1C	3F1ABEFA	01DB8462	3F1E18AE	8400283A	BF1163AC	9D3FC106
(320)	BD5E9E9E	58CD8327	BE711F25	5C6F2781	3E151CUF	5F809AEF	BDDA7986	D8B0BF15	BE725234	5EA71F89
(360)	3FB80450	65AA5183	3F2D1DC3	44566539	3FB7E1E1	30453F53	3E1FF73A	509F16D2	BF100AAF	62564B32
(400)	BF157560	CE4004D1	3F7DAA68	55E886E9	BF229A27	5F2F8ABA	BF1461A7	313F83CA	BDE9458F	F221AC11
(440)	3F2674DA	3504841D	BEBAE25A	0ECBAFF2	3D85DBD3	F08F6F8D	3F2D4797	AD55C15F	BE871C5A	2BAE3218
(480)	3F5F1331	0740870D	BF41F336	C2E7182E	3E8D27FD	43391869	BF109A5E	072159D7	3E71958D	DE137ED9
(520)	BFFF199C	62B80A95	3E3FCDD6	7303732S	3E043271	2C1FC5C6	3F5A5A39	CF04C201	3E1A019C	41CA4498
(560)	3F4A0C5C	2AD7A74A	3F12CE6F	10879270	3F301F4A	55C50746	BF246F86	CD46A964	BE57916D	2D50A775
(600)	BEAC7E0A	310E8AD2	BE6B0637	937363CF	BE80U6DA	FFE4E001	3E13D1D4	AC3B87EC	BE5409FB	3C9B2917
(640)	BE7599A6	C27E0E60	3F2DCBE3	6F7E18E8	8F152DFA	30438116	3E135FFE	70B3D384	3E1EA72E	1981C1A4
(680)	BE5A7490	80231FAF	BFB85FAA	3645BF69	3F75DC7A	2675AF96	3E52F933	5F4F5CAD	BE67A4BD	38617960
(720)	3FAE390F	867CED78	3E23E9A6	90FD4C43	3FC0613B	24FB6478	3E2850AB	953E6432	3E720A77	72AB4B30
(760)	3F1D05E7	06B5D5B9	BE47A960	48746FB6	3F15C502	2D1E9445	3F24E35B	F4BE4574	BF1323D6	96C0A0ED
(800)	3D508467	8D701C82	3F7E42FA	BCC506F3	8F14FCB8	EBC07036	BE749273	98531588	3E2178F7	67D63AAD
(840)	BF974A5A	511800B6	3E68D3A3	2953F5EF	3E26A153	4C8056FF	3E89D8FE	40AA5B27	BD9AB709	F62A40A6
(880)	8E6590F8	71D243D3	8F88FF56	DF40AE10	BFDFED9D	0D6602TA	3E195C9F	C28F2DE9	3E2826A7	EF9F33F6
(920)	BF62B3EA	021FD224	3F751F4D	A5525C0F	3E743C34	00E23102	BE8A8C83	9A0277DF	BDF2E56F	B428E8C3
(960)	3E79B6F3	ABE49F9A	BF32C901	3D67A762	BF236123	6CB3FCE7	BE3178D6	8748F673	3E285A4B	A2AA2F14
(1000)	3F90DEF8	E451EAD9	8F6935A7	A1057CA5	BF43051B	A61C03ED	BF337795	40C1211F	3E830303	7DD0401A
(1040)	3F3D8DF8	B462F545	BF1DC4FF	AB6DB65B	BF8F024B	7B11AF3C	3E592A19	6D8D3A27	3E5FE48F	DB211E45
(1080)	BFA8A6A1	5F2BB7E4	BF1A3356	6539C9E7	BED33427	F8DB6BCD	BFE1F11A	FA104F61	BF757B0C	D1AF8467
(1120)	BF685BA2	F9AF0AB7	BE1F9FE3	9BE5255F	BE3D8405	5A8FUFB8	3F3E40D2	1F838DE1	BF197BB0	633BF000
(1160)	3F114586	8D6F68DF	BF178B40	F7E623E3	BF1D9932	3DC1697F	BF1A27AD	96CD81CD	3E1246E4	39B52F59
(1200)	3F41811D	C37A0556	BE7262D6	18UC46F6	BF22C970	1E075B12	BE4011FF	B4F0C19B	3E2F86E4	5019A76F
(1240)	3F3AB2B9	CA5AFDED	BF93EDC7	5F39B394	3E3F0083	1A0141EC	BE70787B	2FCA25B5	3FCA4614	69A226D4
(1280)	3E85B002	506AB431	3DAA3DC0	0530DE28	3F308756	FD12C92D	3E8DD899	ED394AA3	BE84D770	DB6C913D
(1320)	3FF2F191	A4C301ED	3E5F3C75	E7499FF6	3EA5CD60	CCD240C2	3F3C32A7	CCD650FF	3F2E9198	7E4A8560
(1360)	BF2472F5	CD9F7BDA	BFF345SC	B6F7U06A	BF10CA87	B376FAC5	3EU5517F	3F5D7EFD	BE1903E1	3EEACEDF
(1400)	3F5F7F29	522ABB28	3E628F90	0BC540AD	3F1FF8U8	EBDD61EA	BF157DB9	2A1799B6	BE282ED3	AC450989
(1440)	3F0F11F6	AFB0A4E5	3C200FB3	540D5240F	BE245164	6DA014B6	3F91116F	81A3AC7E	3EBE0357	855217F0
(1480)	BEC763D5	3649FF02	3F127830	2E7CACA9	3F285112	ECFF980F	3F83371F	FBA6EF62	0D9BB17E	312B5C9E
(1520)	3F100B6C	7C75U371	3FBC0F5F	B2E1B32F	3E91100D	EC37AD8C	BE5A09EE	0067685C	3F163137	F070099F
(1560)	3E166BA1	C490BAB6	BFF1AC59	53189A1D	BE2EC2F7	5EEAC713	BE1E221C	AFB6D109	BD26D90D	B8B06CAA
(1600)	BF22F74C	ACDC66AD	BE701BF3	22763775	3FC5EB82	4AF09D3C	3F475917	D51D4B2F	BF7PE352	5A090D78
(1640)	BF2B6E17	CC4886AF	3F40F0U8	224FA473	BE6AB246	58E42E4	BEB685FC	CF016465	3F17F707	55B690C3
(1680)	3F89ED12	55AA947A	BE6D4665	03035B9D	BE560160	9CD918A7	BF28UD9B	160B1E4D	3E1FCB29	C55DE2CE
(1720)	BF171FU1	837831C1	3F1DFA46	EF06EB78	3F24A327	C140F69F	BF118B62	4EA23A25	BE8117A6	5C0F7B29
(1760)	3F4E0F1F	B3582AFA	3F17C6B2	78BE6487	BE659BAC	F3BBD063	BE1CF2E3	035A3B9B	3E83ECB1	91771D58
(1800)	BE5A551F	9D3E6E7B	3E63156E	EB009232	3F13641F	6DA7C747	3E629E09	490908A5	BDA5A1DE	84F38621
(1840)	BDB99911	7D7DF253	1F18C4FB	0E5EE5CF	BF7F94E8	FFFD3F0E	BE78B5C3	2556EA38	3F187205	7A19D791
(1880)	3FF44B37	46BAA068	BFCF9F2A	B6C42372	BEE983C5F	77396514	3E230AAF	B0D7F86B	3D45104E	B4A5FD6F
(1920)	BF37B1F7	1C731CF8	3F69AD57	52B2A4D6	BF374C4A	3CD8DAB3	BFC5D246	79EF9CEA	BE925TE2	9786F524
(1960)	BFAF3D20	0CA2EB91	BD1B30UC	598002F0	BF33B76F	5A100986	BE2FF7A9	4F65C001	3E1ACBF9	54FA1C6E
(2000)	BF4C4CFF	B9AA2E81	BFB06203	5C6CB00C	3D87U8A7	BC953323	BDE99CFD	6B8E3173	3D6B91DB	4F7D490F
(2040)	BF56F7U4	B60BA89D	3F7FF689	C64A2151	3F10435D	09B7E6CF	3D525FD0	BC6CE434	3E1C8523	E72E0A80
(2080)	B57C3224	7EC011A8	BE64AFC8	40A68F3D	3D3778E6	807AF01C	BE376465	74020042	BF16ADD0	D9D5F912
(2120)	3F62F5F3	U20C84C9	3FC1BD16	E7D2A489	3F201692	82C4E60E	8E964B79	9E83C81C	BEF88A5A	4F06F803
(2160)	BFB9B0S1	A0DA941F	3D5AC82D	00000010	00000000	00000000	00000000	00000000	00000000	00000000
(2200)	00000000	00000000	00000000	00000000	00000000	00000000	00000000	00000000	00000000	00000000
(2240)	00000000	00000000	00000000	00000000	00000000	00000000	00000000	00000000	00000000	00000000
(2280)	00000000	00000000	00000000	00000010	00000010	00000000	00000000	00000000	00000000	00000000
(2320)	00000000	00000000	00000000	00000010	00000000	00000000	00000000	00000000	00000000	00000000

(14320)	40C1B9SF	00000000	40C49BA5	00000000	40C353F6	00000000	40BBA5E2	00000000	40B7CED8	00000000
(14360)	40E851EA	00000000	40B60417	00000000	40A7EF9C	00000000	4098S1EA	00000000	408F9DB1	00000000
(14400)	40BB02CB	00000000	408F9DB1	00000000	4086A7EF	00000000	407BDB22	00000000	4067EF9D	00000000
(14440)	40B0C49F	00000000	40BCCCCC	00000000	405EF9DA	00000000	405EF9DA	00000000	4051EB84	00000000
(14480)	40428F5F	00000000	4034TAE1	00000000	402B851F	00000000	4039999B	00000000	404A3D70	00000000
(14520)	405C28F5	00000000	40628F5B	00000000	40620C49	00000000	4089BA5D	00000000	4087EF9D	00000000
(14560)	4088T2AF	00000000	40804168	00000000	407BA5E2	00000000	409C28F5	00000000	40A7EF9C	00000000
(14600)	40B53F7C	00000000	40B70A3C	00000000	40BD70A2	00000000	40B89373	00000000	40A2D0E4	00000000
(14640)	4095SF7C	00000000	40A49BA5	00000000	40A8F5C1	00000000	4077OA3C	00000000	4077CED8	00000000
(14680)	407A0CB9	00000000	405C6A7E	00000000	405TCED8	00000000	4086A7EF	00000000	40991686	00000000
(146C0)	40B35332	00000000	408E3851	00000000	40BBA5E2	00000000	40B74BC5	00000000	40BC28F4	00000000
(14700)	40C147AC	00000000	40C20C48	00000000	40BFFFFF	00000000	40B74BC5	00000000	40A66665	00000000
(14740)	40AC49B9	00000000	4093F7CF	00000000	4086A7EF	00000000	4090E55F	00000000	409374BB	00000000
(14780)	408A3D70	00000000	408F5C28	00000000	409CED90	00000000	408D9167	00000000	4086A7EF	00000000
(147C0)	40BB851E	00000000	405D70A3	00000000	40502DC4	00000000	4054BC6A	00000000	405D70A3	00000000
(14800)	407851EA	00000000	40B872AF	00000000	40A0C49A	00000000	40A2D0E4	00000000	40A66665	00000000
(14840)	409F353F	00000000	40B7CED8	00000000	40BB22D0	00000000	40C51EB7	00000000	40C872AF	00000000
(14880)	40BF7CFC	00000000	40B7CED8	00000000	40A56040	00000000	40989374	00000000	40A5E353	00000000
(148C0)	408BC6A7	00000000	407AE147	00000000	407C6A7E	00000000	407E353E	00000000	407A5E34	00000000
(14900)	407A0CB9	00000000	40A0C49A	00000000	40C56040	00000000	40B60417	00000000	40AE147A	00000000
(14940)	40B53F7C	00000000	40C0C49A	00000000	40C6A7EF	00000000	40C353F6	00000000	40BFB851	00000000
(14980)	40A729D1	00000000	4099DB22	00000000	409A5E34	00000000	40830709	00000000	408D0E55	00000000
(149C0)	4092D0DC	00000000	40A8F5C1	00000000	40A0C49A	00000000	408ED915	00000000	408B020B	00000000
(14A00)	40B353F7	00000000	407C6A7E	00000000	406E5603	00000000	4076872A	00000000	406F5C28	00000000
(14A40)	4077CED8	00000000	4093F7CF	00000000	409E353E	00000000	40818936	00000000	4085E353	00000000
(14A80)	4097DA3C	00000000	40C353F6	00000000	40CA3D6F	00000000	40C72B01	00000000	40C7EF9C	00000000
(14AC0)	40B851EA	00000000	40547AE0	00000000	4091EB84	00000000	40974BC5	00000000	407C28F5	00000000
(14B00)	40574BC6	00000000	4076872A	00000000	407EB851	00000000	406B851E	00000000	40791686	00000000
(14B40)	40AFCFCC	00000000	40C04188	00000000	40C28F5B	00000000	40C28F5B	00000000	40B70A3C	00000000
(14B80)	4089DB21	00000000	40B020C3	00000000	40A41892	00000000	40953F7C	00000000	408B851E	00000000
(14BC0)	40828F5B	00000000	4062D0E4	00000000	40733332	00000000	40866665	00000000	408A3D70	00000000
(14C00)	408BC6A7	00000000	4069374B	00000000	406E147A	00000000	407FFFFF	00000000	40851EB7	00000000
(14C40)	40841B92	00000000	40820C49	00000000	4085E353	00000000	407CED90	00000000	4089374B	00000000
(14C80)	40AF5C28	00000000	40D020C3	00000000	40C04188	00000000	40B6872A	00000000	40B1EB84	00000000
(14CC0)	409F7CEC	00000000	409F7CEC	00000000	40A49BA5	00000000	407851EA	00000000	40866665	00000000
(14D00)	4089374B	00000000	4080C498	00000000	4071EB84	00000000	40851EB7	00000000	40A6A7EE	00000000
(14D40)	40A7AE13	00000000	40A7EF9C	00000000	409CED90	00000000	40A0C49A	00000000	40A147AD	00000000
(14D80)	409DB22C	00000000	408B020B	00000000	4087AE13	00000000	40747AE0	00000000	405AE147	00000000
(14DC0)	40666665	00000000	4072BC20	00000000	407F7CEC	00000000	40804188	00000000	4086A7EF	00000000
(14E00)	40851EB7	00000000	40922D0D	00000000	408C49B9	00000000	40830709	00000000	40872B01	00000000
(14E40)	40AC49B9	00000000	40C9BA5D	00000000	40D4BCB9	00000000	40AC49B9	00000000	40B89373	00000000
(14E80)	408228F5B	00000000	40A28F5B	00000000	40AE147A	00000000	4095C28E	00000000	409AE146	00000000
(14EC0)	4095A5F34	00000000	408F851E	00000000	40804168	00000000	40856040	00000000	40A04188	00000000
(14F00)	40966725	00000000	408147AD	00000000	40AB020B	00000000	409DB22C	00000000	4091EB84	00000000
(14F40)	408CCFCC	00000000	407F353F	00000000	4074BC69	00000000	407EB851	00000000	40799999	00000000
(14F80)	40818936	00000000	40841892	00000000	409020C3	00000000	40953F7C	00000000	409FFFFF	00000000
(14FC0)	40B70A3C	00000000	40D7CED8	00000000	40A6A7EE	00000000	4090E55F	00000000	408E5603	00000000
(15000)	40933332	00000000	40853F7C	00000000	4093F7CE	00000000	40970A3C	00000000	405E353F	00000000
(15040)	406872AF	00000000	4077CED8	00000000	40656041	00000000	406CCCCC	00000000	40A56040	00000000
(15080)	4094BC69	00000000	40933332	00000000	40953F7C	00000000	40974BC5	00000000	40A0C49A	00000000
(150C0)	40B60417	00000000	40CF9DB1	00000000	40A5E353	00000000	4089BA5D	00000000	40A20C48	00000000
(15100)	40CF1479	00000000	40A8F5C1	00000000	406A7EF9	00000000	407D70A3	00000000	407FFFFF	00000000
(15140)	4073F7CE	00000000	4089BA5D	00000000	407C28F5	00000000	40C18936	00000000	40818936	00000000
(15180)	4090E55F	00000000	4092B020	00000000	40CC49B9	00000000	409EF9DA	00000000	408EF9DA	00000000
(151C0)	408F5603	00000000	4082D0E4	00000000	408353F7	00000000	407EB851	00000000	408D0E55	00000000
(15200)	407AE147	00000000	406A3D70	00000000	406B851E	00000000	40893748	00000000	407C28F5	00000000
(15240)	4087642A	20000000	42120000	00000000	00000000	00000000	00000000	00000000	00000000	00000000
(15280)	00000000	00000000	00000000	00000000	00000000	00000000	00000000	00000000	00000000	00000000

1984/177/84